IEEE Robotics and Automation Letters (RA-L) paper, presented at ICRA 2026, Vienna, Austria. Cite as RA-L paper.

Intraoperative Tumor Localization using Sweeping Palpation in Robot-Assisted Minimally Invasive Surgery (RMIS)

Jeongbin Hong, Yunjeong Lee, Youngjun Ryu, Hyoryong Lee, Joowon Park, and Sukho Park, *Member, IEEE*

***Abstract*— Robot-assisted minimally invasive surgery (RMIS) provides superior visualization, precision, and flexibility, and it has gained recognition as a technology that enhances therapeutic outcomes, particularly in tumor resection. However, this technology has a limitation in that it predominantly relies on visual feedback, making it challenging for surgeons to accurately detect the location and edges of tumors during surgery. To address this issue, robotic palpation methods have been actively studied. Among these, the sweeping palpation method has the advantage of rapidly exploring a broad region. Nevertheless, conventional sweeping palpation methods can only roughly identify the tumor's location and are limited in detecting tumor edges with precision. In this study, we introduce a novel sweeping palpation method to overcome the limitations of conventional sweeping palpation in RMIS and propose a precise tumor localization method based on this approach. The proposed method involves performing sweeping palpation on the tissue surface using the tip of the robotic end effector while utilizing a Laplacian edge detection algorithm to detect abrupt changes in contact force. This method reduces the reliance on preoperative imaging and enables tumor localization to be performed within a single robotic system. To validate the proposed tumor localization method, we conducted three phantom experiments and *ex vivo* experiment. These validations demonstrate the potential of our proposed method to contribute to precise tumor resection and the establishment of effective treatment plans.**

***Index Terms*—Sweeping palpation, Tumor localization, Force map, Robot-assisted minimally invasive surgery**

I. Introduction

In recent years, there has been active research on tumor localization in robot-assisted minimally invasive surgery (RMIS), which is characterized by superior visualization, precision, flexibility, and accuracy [1]. Such research plays a crucial role in enabling surgeons to identify the edges between tumor and normal tissues, select appropriate resection points, and thereby establish precise treatment plans and perform accurate tumor resection procedures. In particular, accurately delineating tumor edges contributes to preserving surrounding healthy tissues as much as possible and improving the success rate of tumor resection [2].

Two main methods are commonly used for tumor localization in RMIS. The first method is an image-based tumor localization method that utilizes both preoperative 3D medical images and intraoperative endoscopic images. Here, 3D medical images refer to preoperative scans obtained using CT, MRI, and PET systems [3][4][5]. However, this method has limitations in accurately monitoring the shape of tumors within organs during surgery. For organs composed of soft tissues, tumor localization and spatial coordinate matching based on preoperative images may result in errors due to deformations in organ shape and position caused by ventilation and pneumoperitoneum during surgery [2][6][7]. To address these issues, studies utilizing intraoperative endoscopic images for real-time monitoring have been proposed [8]. Intraoperative endoscopic images can reflect real-time changes in organ deformation or position and have the advantage of not causing additional side effects for patients. However, this approach still faces challenges, including occlusions caused by various objects, image distortion, difficulties in detecting tumors located within organs, and reduced real-time processing speeds [8][9][10].

The second method is tumor localization using robotic palpation. In general, medical palpation is known to be an effective diagnostic method in which physicians use tactile sensation to assess the pathological state of a patient. However, in RMIS, surgeons rely solely on visual feedback during surgery, as they cannot directly touch the patient's soft tissues to obtain tactile feedback [11]. To address this issue, force reflection-based methods have been investigated to identify the mechanical properties of organ tissues by directly measuring force or stiffness through contact with a palpation probe. Representative approaches include individual discrete uniaxial indentation, rolling indentation, and sweeping palpation, each of which has its own limitations. Individual discrete uniaxial indentation can be time-consuming for detecting tumors when a large tissue area needs to be examined [6]. Therefore, lateral indentation methods such as rolling indentation or sweeping palpation have been proposed as more efficient alternatives, as

Manuscript received: February 18, 2025; Revised: May 16, 2025; Accepted: July 4, 2025. This paper was recommended for publication by Editor Pietro Valdastri upon evaluation of the Associate Editor and Reviewers' comments. This work was supported by the National Research Foundation (NRF), funded by the Ministry of Science & ICT (NRF-2021R1A2C3007817), and the Industrial Strategic Technology Devel-opment Program, funded by the Ministry of Trade, Industry & Energy (MOTIE, Korea) (20017903).

The authors are with the MBR Laboratory, Daegu Gyeongbuk Institute of Science and Technology, Daegu 42988, South Korea (e-mail: bsb05028@dgist.ac.kr; yun003102@dgist.ac.kr; ryu0snail@dgist.ac.kr; hr_lee@dgist.ac.kr; pjweng@dgist.ac.kr; shpark12@dgist.ac.kr).

Digital Object Identifier (DOI): see top of this page.

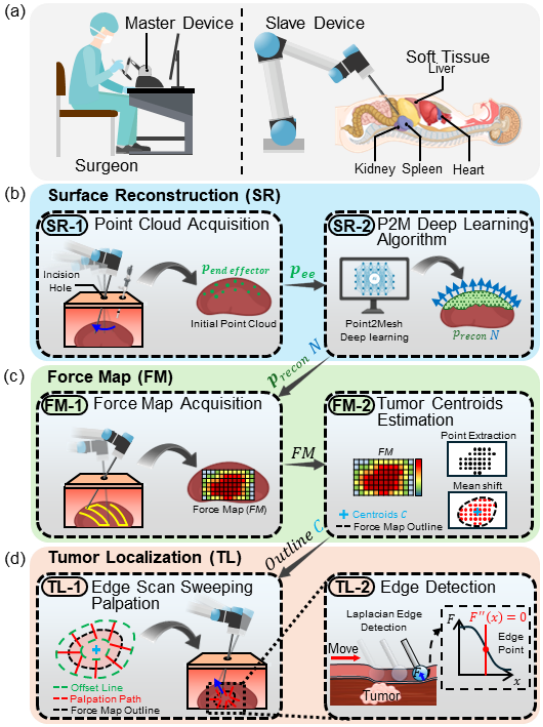

Fig. 1. Overall process of the proposed tumor localization. (a) Concept of the RMIS, (b) Schematic representation of the surface reconstruction, (c) Force map, and (d) Tumor localization.

difficulties in maintaining a consistent indentation depth during palpation [13]. To overcome such limitations, recent studies have explored the reconstruction of organ surfaces to generate effective palpation paths. For this purpose, camera-based imaging techniques [2] or robot-based palpation tools [14] have been utilized. In addition, although conventional force reflection-based palpation methods are effective for roughly localizing tumor regions, they are limited in accurately identifying the edge between tumors and surrounding healthy tissue. Consequently, these limitations hinder their direct application in tumor resection surgeries [15][16][17][18]. To address this, edge estimation techniques based on stiffness variation using sweeping palpation have been proposed. These methods aim to achieve more precise tumor localization by capturing mechanical property changes occurring along tumor edges [19]. Nonetheless, challenges remain in applying these methods to MIS. In particular, the structure and configuration of commonly used sensors are restricted, and actual organs often exhibit curved surfaces, making it difficult to directly apply previous methods developed under the assumption of flat tissue.

To overcome these limitations, we propose an enhanced tumor localization method that builds upon a previously developed image-free sweeping palpation framework. The proposed method reconstructs the surface position and normal vector of the tissue without using medical images, and applies a Laplacian edge detection algorithm to the force profile obtained through sweeping palpation. This allows for more accurate estimation of tumor edges by detecting localized changes in tissue stiffness. By addressing the limitations of they allow rapid exploration of broader regions [12]. However, these methods face
conventional sweeping palpation—particularly the challenges of applying such methods to curved surfaces—our approach improves both the precision and applicability of tumor localization in robot-assisted minimally invasive surgery (RMIS) environments.

II. Method

A. Overall Process of the Proposed Tumor Localization

This study proposes an intraoperative tumor localization method that utilizes the sweeping palpation method and the Laplacian edge detection algorithm to address the aforementioned challenges. As shown in Fig. 1, the proposed tumor localization method for RMIS procedures consists of the following three palpation stages: surface reconstruction (SR), force map (FM), and tumor localization (TL). As depicted in Fig. 1(a), it is assumed that, in RMIS, the surgeon operates on soft tissue via teleoperation using a master device and a slave device. The first palpation procedure, SR (Fig. 1(b)), obtains the initial point cloud (SR-1), which represents the surface position of the soft tissue, $p_{end\ effector}$, in an image-free manner using the coordinates of the robotic end effector. Subsequently, in SR-2 (P2M deep learning algorithm), the initial point cloud data is used to generate a reconstructed surface by applying the Point2Mesh deep learning algorithm. The reconstructed surface includes both the surface position p_{recon} and the surface normal vector N. Here, p_{recon} denotes the 3D coordinates of the surface point, and N indicates the corresponding surface normal vector. In the second palpation procedure, FM (Fig. 1(c)), FM-1 (Force Map Acquisition) generates a sweeping palpation path based on the p_{recon} and N obtained from the reconstructed surface. The robot follows this path to measure the force exerted on the tissue, thereby creating a force map. Next, in FM-2 (Tumor Centroids Estimation), the tumor centroids C and the force map outline are estimated using a mean shift clustering algorithm applied to the force map data.

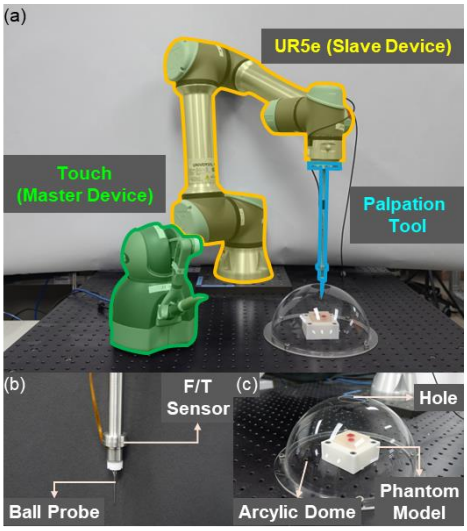

Fig. 2. Robotic palpation system setup. (a) Overall system, (b) Palpation tool, and (c) Phantom experiment setup.

Here, C denotes the estimated 3D positions of the tumor centroids. Finally, in the third palpation procedure, TL (Fig. 1(d)), TL-1 (Edge Scan Sweeping Palpation) generates an edge scan sweeping palpation path based on the C and force map outline estimated in FM-2. The robot performs sweeping palpation along these paths. In TL-2 (Edge Detection), the Laplacian operator is applied to detect the force changes between normal tissue and tumor tissue, which exhibit different stiffnesses, and the final tumor edge is estimated.

B. System Overview

As shown in Fig. 2, the robotic palpation system setup used in this study consists of a master device and a slave device for teleoperation, a tool for performing palpation, and a setup for phantom experiments. As depicted in Fig. 2(a), the master device is a Touch (3D Systems Inc.), and the slave device is a UR5e (Universal Robots A/S). The two devices operate via teleoperation using Xenomai 3.2 kernel on Ubuntu 18.04.01 LTS OS, with control at a loop rate of 2 ms. The palpation tool, shown in Fig. 2(b), is attached to the end effector of the UR5e, and a Hex12 (Resense GmbH) force torque sensor is used. A ball probe with a diameter of 2 mm is mounted at the end of the force torque sensor to maintain a consistent contact area during palpation on soft tissue while minimizing tissue damage. Finally, Fig. 2(c) illustrates the phantom experimental setup, which simulates the RMIS surgical environment. An acrylic dome with a hole on its top surface was used, allowing the palpation tool to be inserted. Therefore, the experiment was conducted by applying remote center of motion (RCM) constraint control.

C. Surface Reconstruction (SR) Procedure

In our previous work, we conducted a study aimed at developing an image-free surgical method applicable to MIS by performing point cloud acquisition and surface reconstruction [14]. Building upon this, the present study generates paths for palpating soft tissue, which are used to perform position control during the FM and TL procedures. As shown in Fig. 1(b), the surface reconstruction (SR) procedure consists of the following two steps. The first step, SR-1 (Point Cloud Acquisition), generates a point cloud to acquire data from the surface of the soft tissue. The second step, SR-2 (Point2Mesh Deep Learning Algorithm), creates a reconstructed surface based on the acquired point cloud.

SR-1, which generates the point cloud of soft tissue, is performed by having the surgeon teleoperate the slave device using the master device to sweep the surface of the soft tissue. During this procedure, the position data of the end effector is collected and stored as a point cloud. As shown in Fig. 3(a), remote center of motion (RCM) constraint control and position-based impedance control are applied during this procedure to prevent damage to the patient and the soft tissue. RCM constraint control is a method used in a minimally invasive surgery (MIS) to control the robot based on a defined virtual point, the RCM, which restricts the movement of the robot

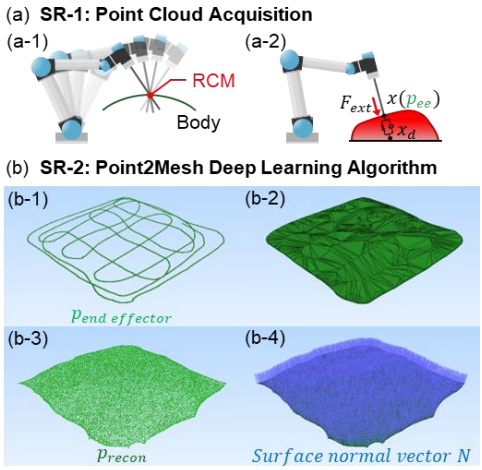

Fig. 3. Surface reconstruction procedure. (a) Point cloud acquisition: (a-1) Remote center of motion (RCM) constraint control and (a-2) Position-based impedance control. (b) Point2Mesh deep learning algorithm: (b-1) Initial point cloud, (b-2) Initial mesh, (b-3) Reconstructed surface, and (b-4) surface normal vector.

when surgical instruments are inserted through an incision hole in the human body [20]. As illustrated in Fig. 3(a-1), this method allows the robot to move while remaining fixed at the incision hole, ensuring safe operation without causing harm to the patient's body. Additionally, as shown in Fig. 3(a-2), position-based impedance control ensures safe operation by controlling the actual position x of the palpation tool at the slave device to maintain appropriate impedance with the soft tissue when a desired position x_d is provided via the master device [21].

Next, in the surface reconstruction procedure, SR-2 focuses on addressing the limitation of point cloud acquisition, which does not include information about areas that were not contacted during the acquisition process. To overcome this limitation, the surface reconstruction was performed using the Point2Mesh deep learning algorithm [22][23]. The Point2Mesh deep learning algorithm is an unsupervised learning method based on a convolutional neural network (CNN) for surface reconstruction. As shown in Fig. 3(b), generating the reconstructed surface requires both the initial point cloud and the initial mesh. The initial point cloud is obtained through the point cloud acquisition step, while the initial mesh is generated using the ball pivoting algorithm based on the initial point cloud [24]. Through this step, data from uncontacted areas is supplemented to create a uniform point cloud of the soft tissue. Based on this uniform point cloud, the reconstructed surface, as illustrated in Fig. 3(b-3) and (b-4), includes both the position p_{recon} and the surface normal vector N.

D. Force Map (FM) Procedure

The proposed force map (FM) procedure is performed based on the reconstructed surface obtained during the surface reconstruction procedure and is utilized to generate paths for the tumor localization (TL) method. As shown in Fig. 1(c) and Fig. 4, the FM procedure consists of two stages: FM-1 (Force Map Acquisition) and FM-2 (Tumor Centroids Estimation).

IEEE Robotics and Automation Letters (RA-L) paper, presented at ICRA 2026, Vienna, Austria. Cite as RA-L paper.

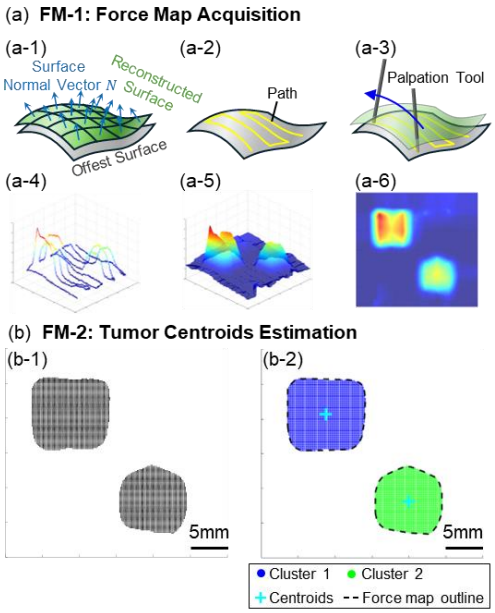

Fig. 4. Force map procedure. (a) Force map acquisition: (a-1) Offset surface generation, (a-2) Path generation, (a-3) Sweeping Palpation, (a-4) Force acquired through sweeping palpation, (a-5) Interpolation of acquired force, and (a-6) Force map (FM) generation. (b) Tumor centroids estimation with clustering: (b-1) Point Extraction and (b-2) Mean shift clustering.

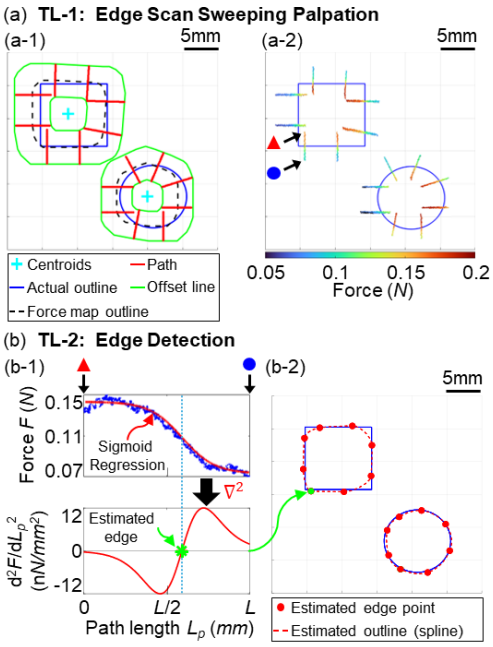

Fig. 5. Tumor localization procedure. (a) Edge scan sweeping palpation: (a-1) Path generation and (a-2) Acquired force from edge scan sweeping palpation. The red triangle and the blue dot represent the start point and the end point of the path, respectively. (b) Edge detection: (b-1) The Laplacian of a sigmoid regression line fitted to the force F with respect to the path length Lp. The green asterisk represents the estimated edge point shown as the green point in (b-2) the result of the edge detection.

The first stage, FM-1 (Force Map Acquisition), involves obtaining force data through sweeping palpation and generating the force map based on this data (Fig. 4(a)). Specifically, as shown in Fig. 4(a-1), an offset surface is created by lowering a fixed depth in the direction of the surface normal vector of the reconstructed surface. Then, as illustrated in Fig. 4(a-2), a path is generated based on the offset surface, and regression lines are placed at regular intervals on the soft tissue. These regression lines are used to extract evenly spaced points, which are then used to create the palpation path. Since the reconstructed surface consists of irregularly arranged points, the area for path generation is defined, and the points within this area are converted into a single regression line using the least squares method [25]. Sweeping palpation is then performed at a fixed depth along the path shown in Fig. 4(a-3), and force data is measured using a force torque sensor. The measured force data is supplemented through interpolation, as shown in Fig. 4(a-4). This interpolation allows for the estimation of force data not only at the palpated locations but also in the uncontacted regions. Based on the interpolated force data, a mesh is created, enabling the visualization of force data, as shown in Fig. 4(a-5). When the visualized force data is represented on the x-y axis, the final force map acquisition becomes possible, as shown in Fig. 4(a-6).

The second stage, as shown in Fig. 4(b), FM-2 (Tumor Centroids Estimation), estimates the tumor centroids using the generated force map. Specifically, as shown in Fig. 4(b-1), the procedure begins by extracting points from the force map. These points are generated by selecting data above the average force value from the force map. Next, a mean-shift clustering algorithm is applied to the extracted points to estimate the tumor centroids. The mean-shift clustering algorithm is an unsupervised learning-based method that performs clustering by exploring areas with high data density [26]. This algorithm operates using kernel density estimation and a probability density function, iteratively shifting each data point toward regions of higher density through the mean-shift operation. In this study, Gaussian kernels were used for clustering. Through this procedure, as shown in Fig. 4(b-2), clustering results are obtained, and the force map outline is created, allowing the tumor centroids to be estimated.

E. Tumor Localization (TL) Procedure

The force map outline is the result of estimating the tumor outline based on the clustered points obtained from the force map procedure. However, the outline acquired through this method depends on the sweeping palpation path and has limitations in accuracy due to interpolation errors occurring during force map generation. To address these limitations, the tumor localization procedure is performed, which consists of two stages: TL-1 (Edge Scan Sweeping Palpation) and TL-2 (Edge Detection), as shown in Fig. 1(d) and Fig. 5.

The first stage, TL-1 (Edge Scan Sweeping Palpation), involves generating an edge scan sweeping palpation path and performing palpation along this path to acquire force data (Fig. 5(a)). Specifically, as shown in Fig. 5(a-1), this stage generates the edge scan sweeping palpation path, which is constructed based on the tumor centroids and force map outline obtained from the FM procedure. An offset line is generated by offsetting the force map outline with respect to the tumor centroids, determining the length of the path. The direction of the path is set according to the normal vector of the force map outline.

IEEE Robotics and Automation Letters (RA-L) paper, presented at ICRA 2026, Vienna, Austria. Cite as RA-L paper.

When the palpation is performed along the generated path, the contact force data along the edge scan sweeping palpation path can be obtained using the force torque sensor, as shown in Fig. 5(a-2).

The second stage, TL-2 (Edge Detection), estimates the tumor edge by applying the Laplacian edge detection algorithm to the force data acquired in TL-1 (Fig. 5(b)). Specifically, as shown in Fig. 5(b-1), the force data obtained in TL-1 is visualized, where the x-axis represents the path length L_p and the y-axis represents the force F. The starting point of L_p is marked by a red triangle in Fig. 5(a-2), while the endpoint is indicated by a blue dot. In this study, the Laplacian edge detection algorithm was applied to estimate the tumor edge from the force data. This algorithm detects edges by identifying points where the second derivative equals zero, a technique commonly used in image processing to highlight regions with rapid intensity changes [27]. In this study, the force variations due to differences in tissue stiffness around the tumor were considered as boundaries, and the Laplacian edge detection algorithm was applied accordingly. However, the Laplacian edge detection algorithm is sensitive to noise. To mitigate this issue, sigmoid regression was used to fit the data, where the sigmoid function effectively captures changes and has the property of producing a single zero-crossing when the second derivative is applied. As shown in Fig. 5(b-1), after fitting the force data using a sigmoid regression line, the Laplacian operation was performed to estimate the tumor edge. The estimated edge is marked by a green asterisk. As shown in Fig. 5(b-2), the estimated edge points along each path are represented by red dots, while the previously estimated green asterisk points are shown as green dots. Finally, the estimated edge points are connected using a spline interpolation method to achieve tumor localization.

F. Evaluation Metrics

In this study, the evaluation metrics commonly used in the field of object detection, sensitivity, specificity, intersection over union (IoU), error region, and error percentage, are employed to assess the estimated outline. To compute the proposed evaluation metrics, true positive (TP), false positive (FP), false negative (FN), and true negative (TN) are defined, as illustrated in Fig. 6(a). Specifically, TP refers to the region that is inside both the actual outline and the estimated outline. FP is the region outside the actual outline but inside the estimated outline, whereas FN is the region inside the actual outline but outside the estimated outline. TN represents the region that is outside both the actual outline and the estimated outline. At this point, TN is defined as the total area of the reconstructed surface obtained through the surface reconstruction (SR) process. Based on these definitions, the evaluation metrics are computed as shown in Fig. 6(b).

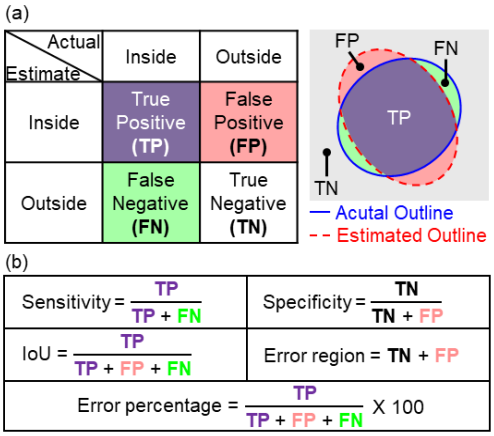

Fig. 6. Evaluation metrics. (a) Definition of True Positive (TP), False Positive (FP), False Negative (FN), and True Negative (TN). (b) Definition of evaluation metircs.

III. Experimental Results & Discussions

A. Phantom Experiments

To evaluate the effectiveness of the proposed tumor localization method, experiments were conducted using three phantom models: planar phantom, curved phantom, and kidney phantom model. The results are presented in Fig. 7(a), (b), and (c), respectively. Each phantom model was fabricated by mixing Ecoflex 00-30 and silicone thinner (Smooth-On Inc.), and the shapes of the models are shown in Fig. 7(a-1), (b-1), and (c-1). During the fabrication of the phantom models, different mixing ratios were used to distinguish the mechanical properties of normal tissue and tumor. The normal tissue, indicated in white, was created by mixing Ecoflex 00-30A, Ecoflex 00-30B, and silicone thinner in a 1:1:1 ratio. The tumor, indicated in red, was fabricated with a 1:1:0 ratio, making it stiffer than the normal tissue. In Fig. 7, the ground truth of the tumor is indicated by the blue line, which is referred to as the "actual outline." The mixing ratios were determined based on previously reported biomechanical data. According to Johnson et al. [28], the elastic modulus of healthy kidney tissue is approximately 30 kPa. In addition, Samur et al. [29] reported that tumor tissues generally exhibit stiffness values that are 2–3 times higher than those of normal tissues. Accordingly, the white region (representing normal tissue) was designed to have a stiffness of approximately 30 kPa, and the red region (representing tumor tissue) was designed to have a stiffness of approximately 60 kPa. The fabricated phantom models were utilized according to the following experimental objectives. The planar phantom model was used for preliminary experiments to validate the feasibility of the proposed tumor localization method. The curved phantom model was designed to evaluate performance on curved surfaces and to verify the effectiveness of the mean-shift clustering algorithm based on various tumor models. Lastly, the kidney phantom model was constructed using actual tumor data obtained from CT scans and was designed to reflect the average size of an adult kidney (10–12 cm) for assessing its potential clinical applicability [28].

IEEE Robotics and Automation Letters (RA-L) paper, presented at ICRA 2026, Vienna, Austria. Cite as RA-L paper.

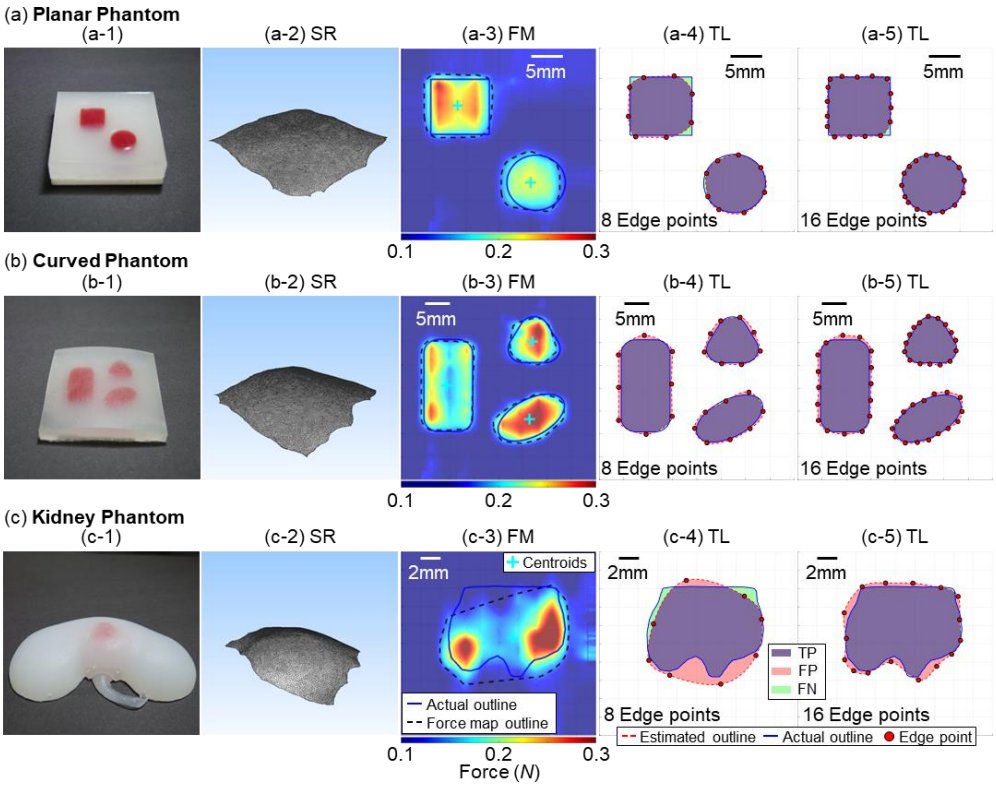

Fig. 7. Phantom experimental results. (a) Planar phantom results: (a-1) Planar phantom model, (a-2) Surface reconstruction, (a-3) Force map, (a-4) Tumor localization for 8 edge points, and (a-5) Tumor localization for 16 edge points. (b) Curved phantom results: (b-1) Curved phantom model, (b-2) Surface reconstruction, (b-3) Force map, (b-4) Tumor localization for 8 edge points, and (b-5) Tumor localization for 16 edge points. (c) Kidney phantom results: (c-1) Kidney phantom model, (c-2) Surface reconstruction, (c-3) Force map, (c-4) Tumor localization for 8 edge points, and (c-5) Tumor localization for 16 edge points.

The experimental results for the three phantom models shown in Fig. 7 can be explained through the three processes: SR (Surface Reconstruction), FM (Force Mapping), and TL (Tumor Localization). For the SR process, Fig. 7(a-2), (b-2), and (c-2) present the results of surface reconstruction performed according to the curvature of the three models. Notably, the curved phantom model and kidney phantom model successfully reconstructed complex surface curvatures. When comparing the data obtained from each experiment with the ground truth, the root mean square error (RMSE) was found to be less than 1 mm in all cases, demonstrating high accuracy. For the FM process, Fig. 7(a-3), (b-3), and (c-3) illustrate the force maps generated for the three models, along with the estimated tumor centroids and force map outline. Experimental results confirmed that tumor centroids were successfully estimated across multiple tumor models, regardless of the number of tumors, and that the force map outline could be generated. However, as seen in the kidney phantom model (Fig. 7(c-3)), obtaining an accurate force map outline for tumors with complex 3D shapes remains challenging. This limitation highlights the necessity of the

subsequent tumor localization (TL) process. For the TL process, Fig. 7(a-4 & a-5), (b-4 & b-5), and (c-4 & c-5) show the results of estimating the tumor edge using force data obtained from edge scan sweeping palpation with 8 and 16 paths, processed through the Laplacian edge detection algorithm. In this process, the edge points for 8 or 16 paths were connected using a spline to derive the estimated outline. The results were quantitatively evaluated using the sensitivity, specificity, IoU, error region, and error percentage described in Section II.E. This quantitative evaluation was performed with reference to the blue line (actual outline) shown in Fig. 7, and the corresponding results are summarized in Table I. The findings indicate that using 16 paths provided a more detailed tumor shape and improved accuracy compared to using 8 paths. In particular, the planar phantom model and curved phantom

TABLE I
EVALUATION METRICS FOR PHANTOM EXPERIMENTS

Phantom model	Num of Paths	Sensitivity	Specificity	IoU	Error Region (mm^2)	Error Percent (%)
Planar	8	0.9556	0.9953	0.9221	13	7.8
	16	0.9833	0.9951	0.9475	9	5.3
Curved	8	0.9913	0.9752	0.8900	45	11.0
	16	0.9978	0.9753	0.8959	42	10.4
Kidney	8	0.9342	0.9835	0.7813	24	21.9
	16	0.9922	0.9896	0.8827	12	11.7

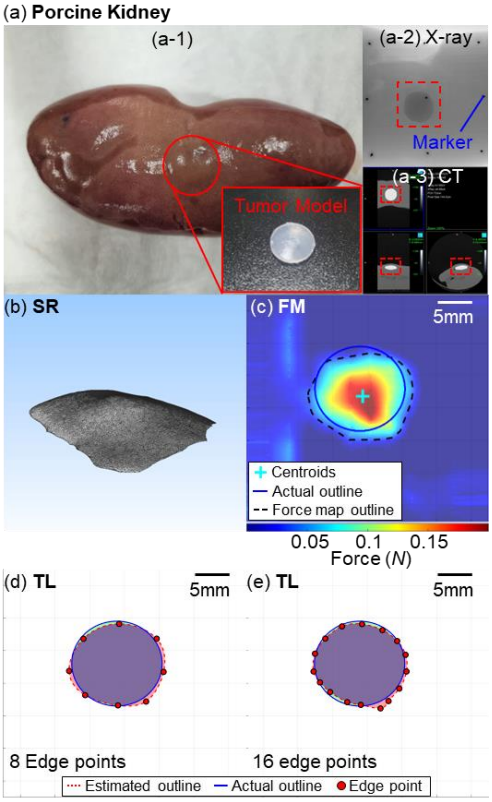

Fig. 8. *Ex vivo* experimental results. (a) Tumor model in porcine kidney (An agarose gel disk was inserted into a porcine kidney): (a-1) Camera image, (a-2) X-ray and (a-3) CT images for ground truth acquisition. (b) Surface reconstruction. (c) Force map. (d) Tumor localization for 8 edge points. (e) Tumor localization for 16 edge points.

model exhibited minor differences in accuracy due to their regular shapes, whereas the kidney phantom model demonstrated higher accuracy as the number of paths increased, reflecting its more complex geometry. Compared to previously reported sensitivity (0.95–0.99) and specificity (0.92–0.97) values [19][30] from phantom experiments, the proposed method in this study demonstrated comparable or even superior performance, consistently achieving high accuracy across all experiments.

B. Ex Vivo Experiment

To validate the applicability of the proposed tumor localization method to real soft tissue, an *ex vivo* experiment was conducted using a porcine kidney. As shown in Fig. 8(a-1), the tumor model used in the *ex vivo* experiment was fabricated by mixing agarose gel, contrast medium, and deionized (DI) water in a 1:3:22 ratio [19]. To clearly establish

the ground truth, the tumor model was mixed with a contrast medium and then scanned using Micro CT (Quantum, Perkin Elmer Inc.) to obtain X-ray and CT images, as shown in Fig. 8(a-2) and Fig. 8(a-3). Subsequently, ImageJ and MATLAB were used along with marker-based analysis to determine the ground truth of the tumor model within the kidney. Based on this, the evaluation metrics were computed for the *ex vivo* experiment.

As illustrated in Fig. 8, the results of the *ex vivo* experiment demonstrated that the proposed tumor localization method could accurately estimate the tumor position and edge through the SR, FM, and TL processes. Based on these results, the evaluation metrics for the *ex vivo* experiment are summarized in Table II.

C. Discussion on Edge Detection

In this study, the Laplacian edge detection algorithm was used for tumor edge detection in tumor localization. However,

since the Laplacian edge detection algorithm is highly sensitive to noise, sigmoid regression line fitting was applied to estimate the tumor edge. Nevertheless, using the sigmoid regression line may introduce distortion in the original data. Various edge detection algorithms exist, and one possible approach to reducing noise is applying a Gaussian smoothing filter. Additionally, modifying the edge detection algorithm itself is another viable approach. For instance, incorporating the Canny edge detection algorithm, which is widely used in edge detection, could leverage its strong resistance to noise, leading to more accurate edge estimation [31]. Applying these methods is expected to enhance the performance of edge detection and further improve the accuracy of the proposed tumor localization method.

D. Discussion on Friction Effects during Sweeping Palpation

In this study, the proposed tumor localization method using sweeping palpation successfully performed tumor edge estimation within soft tissue. However, further analysis and improvement of the sweeping palpation process are deemed necessary. During the sweeping palpation process, the palpation tool remains in contact with the soft tissue and is influenced by frictional forces. In particular, soft tissues such as the liver, heart, kidney, and spleen, which are known to exhibit viscoelastic properties. These characteristics can significantly affect the measurement of contact force between the palpation tool and the soft tissue due to the frictional forces generated during sweeping palpation. Carbone et al. analyzed the frictional forces that occur during sliding (sweeping) motions in viscoelastic materials [32]. Their study indicated that the shape of the contact area and pressure distribution can vary depending on the sliding velocity, which may influence the force data obtained during sweeping palpation. In this study, the sweeping palpation speed was set to 1 mm/s. However, the relationship between velocity and frictional forces was not thoroughly analyzed. Future research should evaluate the

TABLE II
EVALUATION METRICS FOR *EX VIVO* EXPERIMENTS

Phantom model	Num of Paths	Sensitivity	Specificity	IoU	Error Region (mm^2)	Error Percent (%)
Ex vivo	8	0.9638	0.9946	0.9019	14	9.8
	16	0.9484	0.9963	0.9057	13	9.4

performance of tumor localization under varying sweeping palpation speeds to enhance the reliability of this technique. Additionally, a detailed analysis of frictional forces could enable the correction of contact force data, which can then be incorporated into edge detection, ultimately improving the accuracy of tumor localization.

IV. Conclusion

This study proposed a novel sweeping palpation-based tumor localization method to overcome the limitations of tumor localization in soft tissue during RMIS. The proposed method applies to RMIS and utilizes a robotic end-effector equipped with a force torque sensor. The process involves acquiring the point cloud of the soft tissue through the surface reconstruction, followed by the sweeping palpation to generate a force map. Subsequently, the Laplacian edge detection was performed using the force data obtained from the edge scan sweeping palpation, enabling the tumor edge estimation and tumor localization. The feasibility of the proposed method was validated through the three phantom experiments (planar, curved, and kidney phantoms), demonstrating high accuracy in estimating both tumor edges and tumor localization. Additionally, the *ex vivo* experiment using a porcine kidney confirmed the applicability of the proposed sweeping palpation-based tumor localization method to soft tissue. Future research will focus on enhancing the clinical applicability of the proposed tumor localization method by enhancing the edge estimation process and incorporating frictional force analysis. This study is expected to expand the utility of sweeping palpation-based techniques and contribute to the development of precise tumor resection and treatment planning.

References

[1] M. Mir et al., "A Minimally Invasive Robotic Tissue Palpation Device," *IEEE Trans. Biomed. Eng.*, vol. 71, no. 6, pp. 1958-1968, June 2024.

[2] N. Marahrens, D. Jones, N. Murasovs, C. S. Biyani, and P. Valdastri, "An Ultrasound-Guided System for Autonomous Marking of Tumor Boundaries During Robot-Assisted Surgery," *IEEE Trans. Med. Robot. Bionics*, vol. 6, no. 4, pp. 1699-1712, Nov. 2024.

[3] G. Santini, N. Moreau, and M. Rubeaux, "Kidney tumor segmentation using an ensembling multi-stage deep learning approach. A contribution to the KiTS19 challenge," *arXiv*, 2019, arXiv:1909.00735.

[4] S. Gul, M. S. Khan, A. Bibi, A. Khandakar, M. A. Ayari, and M. E. Chowdhury, "Deep learning techniques for liver and liver tumor segmentation: A review," *Comput. Biol. Med.*, vol. 147, p. 105620, 2022.

[5] P. Kumar et al., "Surgeon perception of factors affecting the efficiency of conventional and robotic laparoscopy: A Pan India study," *Heliyon*, vol. 8, no. 12, 2022.

[6] H. Liu, J. Li, X. Song, L. D. Seneviratne, and K. Althoefer, "Rolling Indentation Probe for Tissue Abnormality Identification During Minimally Invasive Surgery," *IEEE Trans. Robot.*, vol. 27, no. 3, pp. 450-460, June 2011.

[7] P. A. Wise, A. A. Preukschas, and E. Özmen, "Intraoperative liver deformation and organ motion caused by ventilation, laparotomy, and pneumoperitoneum in a porcine model for image-guided liver surgery," *Surg. Endosc.*, vol. 38, pp. 1379–1389, 2024.

[8] M. Jiang et al., "MDSK-Net: Multi-scale dynamic segmentation kernel network for renal tumour endoscopic image segmentation," *IET Image Process.*, 2024.

[9] R. Wei et al., "Absolute Monocular Depth Estimation on Robotic Visual and Kinematics Data via Self-Supervised Learning," *IEEE Trans. Autom. Sci. Eng.*, 2024.

[10] T. Rueckert, D. Rueckert, and C. Palm, "Methods and datasets for segmentation of minimally invasive surgical instruments in endoscopic images and videos: A review of the state of the art," *Comput. Biol. Med.*, p. 107929, 2024.

[11] Z. Zhou et al., "Depth Recognition of Hard Inclusions in Tissue Phantoms for Robotic Palpation," *Proc. IEEE Int. Conf. Real-Time Comput. Robot. (RCAR)*, Guiyang, China, 2022, pp. 87-92.

[12] K. Hamamoto, "Investigation on Virtual Palpation System using Ultrasonic Elasticity Imaging," in Proceedings of the 28th IEEE EMBS Annual International Conference, 2006, vol. 1, pp. 4873 4876.

[13] M. Li, H. Liu, A. Jiang et al., "Intra-operative tumour localisation in robot-assisted minimally invasive surgery: A review," Proc. Inst. Mech. Eng. H, vol. 228, no. 5, pp. 509–522, 2014.

[14] S. W. Bang, Y. J. Lee, and H. Kee, "Registration-free Minimally Invasive Surgery Without Preoperative Phase," Int. J. Control Autom. Syst., vol. 21, pp. 3313–3323, 2023.

[15] R. Uppuluri, A. Bhattacharjee, S. Anwar, and Y. She, "SeeBelow: Sub-dermal 3D Reconstruction of Tumors with Surgical Robotic Palpation and Tactile Exploration," Proc. IEEE/RSJ Int. Conf. Intell. Robots Syst. (IROS), Abu Dhabi, United Arab Emirates, 2024, pp. 6961-6968.

[16] C. Hou et al., "A highly integrated 3D MEMS force sensing module with variable sensitivity for robotic-assisted minimally invasive surgery," Adv. Funct. Mater., vol. 33, no. 43, pp. 1–13, Oct. 2023.

[17] A. Talasaz and R. V. Patel, "Remote palpation to localize tumors in robot-assisted minimally invasive approach," 2012 IEEE International Conference on Robotics and Automation, Saint Paul, MN, USA, 2012, pp. 3719-3724.

[18] B. Ahn, H. Lee, Y. Kim, and J. Kim, "Robotic system with sweeping palpation and needle biopsy for prostate cancer diagnosis," Int. J. Med. Robot. Comput. Assist. Surg., vol. 10, pp. 356–367, 2014.

[19] Y. Yan and J. Pan, "Fast Localization and Segmentation of Tissue Abnormalities by Autonomous Robotic Palpation," *IEEE Robot. Autom. Lett.*, vol. 6, no. 2, pp. 1707-1714, Apr. 2021.

[20] N. Hogan, "Impedance Control: An Approach to Manipulation," *1984 American Control Conference*, San Diego, CA, USA, 1984, pp. 304-313.

[21] R. C. O. Locke and R. V. Patel, "Optimal Remote Center-of-Motion Location for Robotics-Assisted Minimally-Invasive Surgery," *Proceedings 2007 IEEE International Conference on Robotics and Automation*, Rome, Italy, 2007, pp. 1900-1905.

[22] R. Hanocka et al., "Point2Mesh: A self-prior for deformable meshes," *ACM Trans. Graph.*, vol. 39, no. 4, Jul. 2020, Art. no. 126.

[23] R. Hanocka, "Point2Mesh: A self-prior for deformable meshes," GitHub repository, Available: https://github.com/ranahanocka/point2mesh, Accessed: May 15, 2025.

[24] F. Bernardini et al., "The ball-pivoting algorithm for surface reconstruction," *IEEE Trans. Vis. Comput. Graph.*, vol. 5, no. 4, pp. 349-359, Oct.-Dec. 1999.

[25] A. Masood et al., "Tool Path Generation for Complex Surface Machining Using Point Cloud Data," *Proc. 12th Global Conf. Sustain. Manuf.*, vol. 26, pp. 397-402, 2015.

[26] K. G. Derpanis, "Mean shift clustering," Lecture Notes, 2005.

[27] X. Wang, "Laplacian Operator-Based Edge Detectors," in IEEE Transactions on Pattern Analysis and Machine Intelligence, vol. 29, no. 5, pp. 886-890, May 2007.

[28] B. Johnson, S. Campbell, and N. Campbell-Kyureghyan, "Characterizing the material properties of the kidney and liver in unconfined compression and probing protocols with special reference to varying strain rate," *Biomechanics*, vol. 1, no. 2, pp. 264–280, 2021.

[29] E. Samur, M. Sedef, C. Basdogan, L. Avtan, and O. Duzgun, "A robotic indenter for minimally invasive characterization of soft tissues," *Int. Congr. Series*, vol. 1281, pp. 713–718, May 2005.

[30] K. A. Nichols and A. M. Okamura, "Methods to Segment Hard Inclusions in Soft Tissue During Autonomous Robotic Palpation," *IEEE Trans. Robot.*, vol. 31, no. 2, pp. 344-354, Apr. 2015.

[31] W. Rong, Z. Li, W. Zhang and L. Sun, "An improved Canny edge detection algorithm," *2014 IEEE International Conference on Mechatronics and Automation*, Tianjin, China, 2014, pp. 577-582.

[32] G. Carbone and C. Putignano, "A novel methodology to predict sliding and rolling friction of viscoelastic materials: Theory and experiments," *J. Mech. Phys. Solids*, vol. 61, no. 8, pp. 1822-1834, 2013.